

1 Study on the vertical ultrasonic vibration-assisted nanomachining 2 process on single-crystal silicon

3 Jiqiang Wang^{1,2}, Yanquan Geng^{1,2}, Zihan Li², Yongda Yan^{1,2,*}, Xichun Luo³, Pengfei Fan³

4 ¹ *The State Key Laboratory of Robotics and Systems, Robotics Institute, Harbin Institute of
5 Technology, Harbin, Heilongjiang 150080, PR China*

6 ² *Center for Precision Engineering, Harbin Institute of Technology, Harbin, Heilongjiang 150001,
7 P.R. China*

8 ³*Centre for Precision Manufacturing, Department of Design, Manufacture and Engineering
9 Management, University of Strathclyde, Glasgow, UK.*

10 * *Corresponding author. Tel.: +86-0451-86412924. Fax: +86-0451-86415244*

11 *E-mail address: yanyongda@hit.edu.cn (Y. D. Yan)*

12

13

Abstract

14 Subsurface damage that is caused by mechanical machining is a major impediment to
15 the widespread use of hard–brittle materials. Ultrasonic vibration-assisted macro- or
16 micromachining could facilitate shallow subsurface damage compared with
17 conventional machining. However, the subsurface damage that was induced by
18 ultrasonic vibration-assisted nanomachining on hard–brittle silicon crystal has not yet
19 been thoroughly investigated. In this study, we used a tip-based ultrasonic vibration-
20 assisted nanoscratch approach to machine nanochannels on single-crystal silicon, to
21 investigate the subsurface damage mechanism of the hard–brittle material during
22 ductile-machining. The material removal state, morphology, and dimensions of the

1 nanochannel, and the effect of subsurface damage on the scratch outcomes were studied.
2 The materials were expelled in rubbing, plowing, and cutting mode in sequence with
3 an increasing applied normal load and the silicon was significantly harder than the
4 pristine material after plastic deformation. Transmission electron microscope analysis
5 of the subsurface demonstrated that ultrasonic vibration-assisted nanoscratching led to
6 larger subsurface damage compared with static scratching. The transmission electron
7 microscopy results agreed with the Raman spectroscopy and molecular dynamic
8 simulation. Our findings are important for instructing ultrasonic vibration-assisted
9 machining of hard–brittle materials at the nanoscale level.

10 **Keywords:** vibration-assisted nanoscratch, single-crystal silicon, subsurface damage

11 **1. Introduction**

12 Increased focus has been given to the use of hard–brittle materials, such as single-
13 crystal silicon, owing to their excellent physical and mechanical properties [1,2].
14 Nanostructures on silicon-based materials are used extensively in many fields [3,4].
15 Several approaches have been used to fabricate micro- and nanostructures on silicon,
16 such as reactive-ion etching, focused ion-beam lithography, and electron-beam
17 lithography [5-7]. However, these methods are limited by disadvantages, such as a high
18 facility cost, strict environmental requirements, and a low processing efficiency.

19 Mechanical machining is a more powerful and feasible method to machine single-
20 crystal silicon [8,9]. However, subsurface damage results because of the tool–
21 workpiece contact during machining, which affects the mechanical, electronic, and
22 optical performance of silicon-based devices. Ultrasonic vibration-assisted machining

1 (UVM) is used extensively to suppress the propagation of subsurface damage. UVM
2 facilitates shallow subsurface damage compared with conventional machining [10-14].
3 Many researchers have reported that UVM improves the critical depth of the brittle–
4 ductile transition, reduces the scratch load, and inhibits microcrack propagation [15,16].
5 However, the depth of material removal for the UVM process mentioned above was at
6 the macro- or microscale. To the best of the authors’ knowledge, UVM with a nanoscale
7 machined depth has not been conducted on hard–brittle materials (such as silicon), and
8 the subsurface damage mechanism that caused by nanoscale-UVM has not been
9 investigated.

10 Atomic force microscopy (AFM) tip-based nanoscratching has been proven as a
11 powerful technique to machine structures with a nanoscale depth of material removal
12 [17,18]. Thus, this technique is suitable for investigating the subsurface damage
13 mechanism of single-crystal silicon at the nanoscale. Lee [19] conducted conventional
14 tip-based nanoscratching on silicon. The machining characteristics and brittle–ductile
15 transitions were monitored by using acoustic emission approach. However, the
16 subsurface damage that was caused by nanoscratching was not studied. Qian et al. [20]
17 achieved the nondestructive fabrication of nanochannels on silicon using a tip-based
18 tribochemistry induced direct nanomachining approach. Wang et al. [21] investigated
19 the subsurface damage of single-crystal silicon that was induced by tip-based
20 nanomilling. They revealed the subsurface, including many dislocations, stacking faults
21 and a layer of amorphous silicon. Nevertheless, the nanomilling was close to
22 conventional tip-based nanomachining rather than ultrasonic vibration-assisted

1 nanomachining. A vertical Z-axis vibration-assisted tip-based machining approach was
2 carried out by Park et al. [22] to fabricate nanochannels on a gold layer. The method
3 could increase the groove depth significantly. Dong et al. [23,24] fabricated three-
4 dimensional nanostructures on polymethyl methacrylate samples with the aid of
5 ultrasonic tip-sample Z-vibration. A tip-based scratching method with vertical Z-axis
6 vibration was used by Geng et al. [25] to machine the polymer resist. A deeper
7 machined depth and less tip wear were observed compared with the conventional
8 machining technique. However, in contrast with polymers, single-crystal silicon was
9 brittle with little ductility during machining, which makes it difficult to machine. Tip-
10 based ultrasonic vibration-assisted nanoscratching (UVS) that is conducted directly on
11 silicon has not been investigated, and the induced subsurface damage is unclear. Thus,
12 the machining characteristics (i.e., the mechanism of material removal and subsurface
13 damage) should be thoroughly understood for using UVS on single-crystal silicon.

14 The objective of this study was to investigate nanochannel machining on single-
15 crystal silicon using a tip-based UVS approach. This paper is structured as follows.
16 Section 2 describes the experimental details, and includes the machining setup and
17 molecular-dynamics (MD) simulation model. Section 3 analyzes and compares the
18 machining outcomes (i.e., the mechanism of material removal and subsurface damage)
19 of nanochannels that were fabricated by using UVS and static scratching, respectively.
20 By using a double-pass scratch approach, the effect of subsurface damage on the
21 machining mechanism was investigated. The main conclusions are given in Section 4.
22 Our findings are significant for understanding the mechanism of subsurface damage

1 that is caused by ultrasonic vibration-assisted nanomachining on hard–brittle material.

2 **2. Experimental details**

3 **2.1 Setup and methods**

4 A commercial AFM with a Nanoscope-V controller (Dimension Icon, Bruker
5 Company, Germany) was used to conduct the fabrication experiments. Figure 1(a)
6 shows a schematic diagram of the AFM-based UVS setup. The sample was attached to
7 a piezoelectric actuator (OD12-F2MHz, Core Tomorrow Science & Technology Co.,
8 Ltd., China) with the aid of vacuum grease to avoid vibration energy dissipation. The
9 piezoelectric actuator achieved a megahertz-level vibration in the vertical Z-axis
10 direction under the action of a driving signal that was generated from a commercial
11 signal generator (AFG1022, Tektronix, USA). Figure 1(b) and (c) provides scanning
12 electron microscopy (SEM) micrographs and schematic diagrams of the triangular
13 pyramidal diamond tip (PDNISP, Bruker, Germany) that conducted the machining. The
14 geometric angles of the tip, such as a side (θ_s), back (θ_b), and front (θ_f) angle, as shown
15 in Figure 1(d) and (e), are 51° , 35° , and 55° , respectively. The normal spring constant
16 (K_N) and resonance frequency of the tip cantilever that were provided by the
17 manufacturer were 286 N/m and 69.2 KHz, respectively. The tip radius (R) was ~86
18 nm as evaluated by the blind tip reconstruction approach using a titanium roughness
19 sample (RS-15 M, Bruker, Germany). The estimated normal load that was applied on a
20 sample by the tip is:

$$21 \quad F_N = V_{\text{setpoint}} \cdot \textit{Sensitivity} \cdot K_N \quad (1)$$

22 where V_{setpoint} is the voltage of the laser on the photodetector that was set before the

1 scratching process. The sensitivity of the light lever system can be obtained from the
2 slope of the force–distance curve when the tip presses onto a hard sapphire sample
3 (SAPPHIRE-15 M, Veeco, USA). The normal loads that were used in this study ranged
4 from 50 μN to 300 μN with a spacing of 50 μN . The samples that were used in this
5 study were single-crystal silicon (100) wafers (Suzhou Research Semiconductor Co.,
6 Ltd., China), which were polished on a single side. The measured surface root-mean-
7 square roughness of the sample was ~ 0.1 nm by scanning a $1\ \mu\text{m} \times 1\ \mu\text{m}$ area using the
8 AFM. To compare the effects of tip-based static and UVS on the subsurface damage,
9 three methods for nanochannel fabrication that were investigated in detail are static
10 scratch (SS) (Figure 1(f)), UVS (Figure 1(g)), and double-pass scratch (Figure 1(h)).
11 These three nanochannel fabrication approaches are described below.

12 (1) SS approach

13 As shown in Figure 1(f), the AFM system was operated in Nanoman mode and the
14 tip was set to machine the sample only once. In the SS approach, no driving signal was
15 generated from the signal generator during machining, thus, the sample was static
16 during the scratching. The scratch direction was selected as the side-forward direction
17 along the $[\bar{1}\ \bar{1}\ 0]$ crystal orientation.

18 (2) UVS approach

19 Ultrasonic vibration was applied in the vertical direction with a piezoelectric
20 actuator under the drive of a sinusoidal signal (Figure 1(g)). The dynamic behavior of
21 the piezoelectric actuator was investigated based on a microscope and microparticles.
22 Some microparticles were placed on the sample surface to observe their motion by

1 using the microscope when the piezoelectric actuator conducted ultrasonic vibration.
2 By monitoring the microparticle motion and distribution, an appropriate excitation
3 frequency can be found that ensures that the sample is vibrated with a maximum
4 vibrational amplitude, which was 0.2 MHz in this study. The vibration amplitude of the
5 piezoelectric actuator was 1.5 nm as tested by the AFM system. The excitation
6 frequency of the driving signal was larger than the resonance frequency of the tip
7 cantilever, and thus, the cantilever dynamically ‘freezes’ because of its inertia and the
8 tip does not vibrate with the sample during UVS [24]. The tip pressed into the sample
9 with a preset normal load and scratched along a linear trajectory while the piezoelectric
10 actuator produced an ultrasonic vibration.

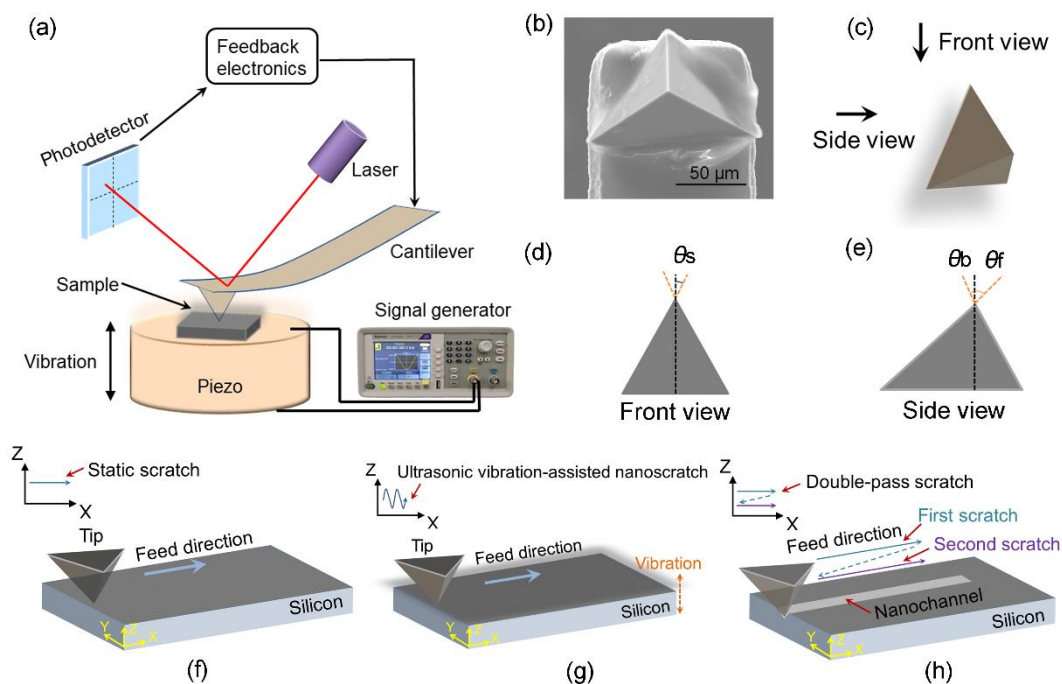
11 (3) Double-pass scratch approach

12 Figure 1(h) provides a schematic diagram of the double-pass scratch process. The
13 double-pass scratch approach was carried out using the Nanoman mode of the AFM
14 system. Two different machining methods—the SS and UVS—were used in the first
15 scratch process. When the first scratching finished, the tip returns to the initial position
16 under PZT control in tapping mode, which guarantees an interaction force between the
17 tip and sample to protect the nanochannel morphology. The AFM system changed to
18 contact mode again to repeat the SS process during the second scratch.

19 The morphologies of the obtained nanochannels were measured by SEM (Quanta
20 200FEG, FEI, USA) and AFM (Dimension Icon, Bruker, Karlsruhe, Germany). The
21 SEM measurement was conducted immediately after scratching without further
22 treatment. To remove the generated chips, the sample was scanned with a silicon AFM

1 tip in contact mode with a relatively small normal load and cleaned ultrasonically in
 2 alcohol for 10 min. A new silicon tip (TESPA, Bruker, Germany) was used to measure
 3 the topographies of the nanochannels in tapping mode. A commercial Renishaw Raman
 4 system (InVia-Reflex, Renishaw, England) was used to characterize the material
 5 structural changes. The laser wavelength was 633 nm and the laser beam power was
 6 1.7 mW. The objective lens and typical accumulation parameters were 100× and 10 s,
 7 respectively. The subsurface characteristics of the machined structures were observed
 8 by transmission electron microscopy (TEM) (FEI Tecnai F20, USA). Cross-sectional
 9 TEM samples were prepared by using a focused-ion beam (FIB, FEI Helios NanolabG3
 10 UC, USA), and the samples were thinned to ~90 nm to enable electron transmission. A
 11 protected layer (Pt) on the machined nanostructures was coated before TEM sample
 12 preparation to avoid sample surface and subsurface damage that was induced by FIB.

13



14

15

Figure 1. (a) Schematic of AFM-based UVS setup, (b) SEM micrograph and (c)

1 schematic of diamond AFM tip. (d,e) Schematic diagrams of side and front views of
2 diamond tip. Schematic representation of (f) static scratch, (g) ultrasonic vibration-assisted
3 scratch, and (h) double-pass scratch.

4 **2.2 MD simulation model**

5 Figure 2 shows the MD simulation model of the UVS approach. The inclination
6 angle ($\sim 12^\circ$) of the tip was subject to the mounting angle of the tip cantilever. The
7 single-crystal silicon substrate contained 129271 Si atoms and a single diamond AFM
8 tip was modeled as a rigid body. The feature dimensions of the substrate were $38 \text{ nm} \times$
9 $22 \text{ nm} \times 14 \text{ nm}$. The Si atoms were arranged in a diamond cubic lattice structure with
10 a lattice constant of 5.428 \AA . As shown in Figure 2, the workpiece was categorized into
11 three parts: boundary, thermostat, and Newtonian atoms. Boundary atoms were used to
12 reduce the boundary effect and maintain the proper lattice symmetry. Thermostat atoms
13 were kept at a constant 293 K. The Stillinger–Weber potential function was used to
14 calculate the interatomic forces between the Si–Si atoms, which was an appropriate
15 potential for the simulation of covalent bonding materials [26]. The interaction between
16 the tip and sample atoms (C–Si) was expressed by the Morse potential [27]. The initial
17 velocities of the Si atoms were assigned in accordance with the Maxwell–Boltzmann
18 distribution and the model was equilibrated to 293 K under the canonical ensemble
19 (NVT) in 50 ps. The vibrational amplitude of the sample and tip feed rate were 5 \AA and
20 2 m/s . The vibrational frequency was 20 GHz in this model to depict the sample
21 vibration. Other simulation details of the model are listed in Table 1. A large-scale
22 atomic/molecular massively parallel simulator was used to conduct the MD simulation
23 [28], and the simulation results were visualized using OVITO software [29].

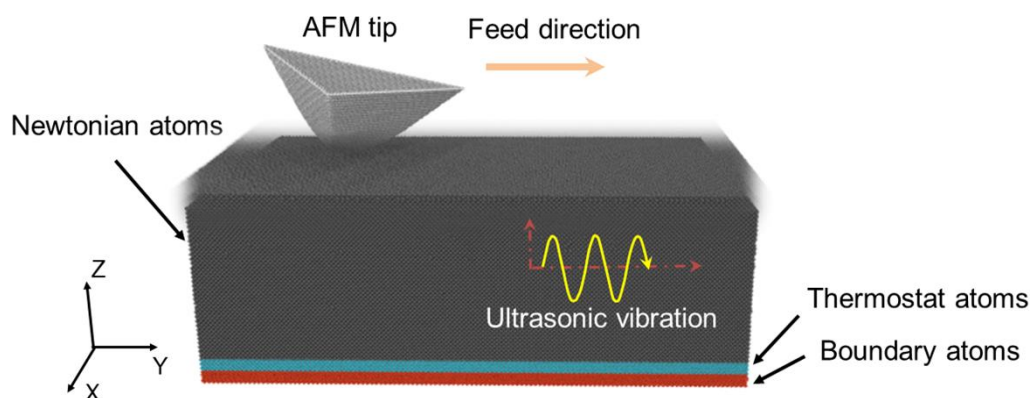


Figure 2. Three-dimensional MD simulation model.

Table 1 MD simulation parameters

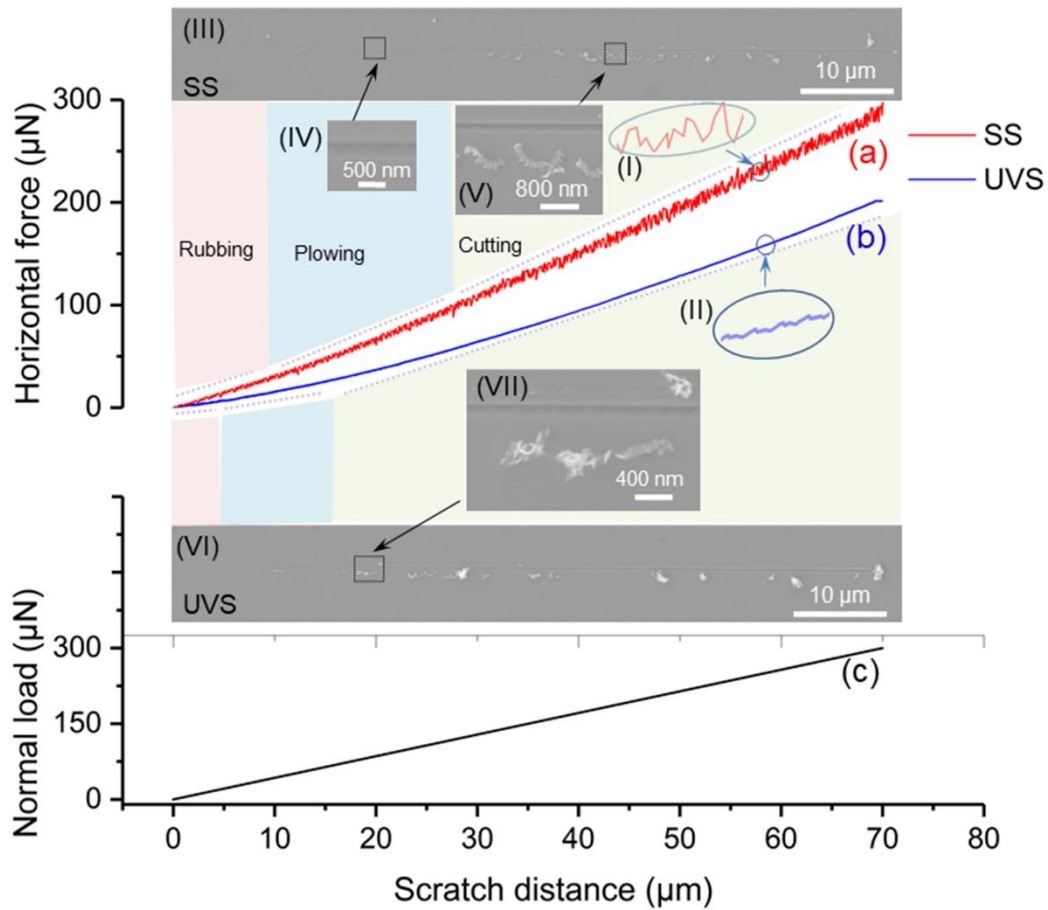
Parameters	Value
Workpiece size	38 nm × 22 nm × 14 nm
Atoms in workpiece	129271
Atoms in tool	4427
Feed rate	2 m/s
Machining distance	20 nm
Amplitude	5 Å
Equilibration temperature	293 K
Time step	1 ps

3. Results and discussion

3.1 Investigation of material removal state

As a hard brittle material, single-crystal silicon will be removed in the brittle regime and cracks, material peeling, or debris will be induced when the machined depth reaches a critical value for the brittle-to-ductile transition depth [19]. Thus, the material removal state is key for studying nanomachining on single-crystal silicon. Figure 3 shows the normal load-horizontal force-distance curves that were acquired in the SS and UVS tests at 3 $\mu\text{m/s}$, where the range of the normal load was set from 0 μN to 300 μN . Curves (a) and (b) in Figure 3 show the relationship between the horizontal force and the scratching distance when scratching using the SS and UVS approach,

1 respectively. The horizontal force for SS was larger than that for UVS. By comparing
2 the horizontal forces in enlarged images I and II in Figure 3, it can be seen that the
3 fluctuation in SS exceeds that in UVS. Curve (c) represents the applied normal load
4 during scratching. Inserted images III and VI in Figure 3 show the SEM images that
5 correspond to nanochannels that were machined by SS and UVS, respectively. An
6 inspection of the horizontal force curves (a) and (b) that were recorded during loading
7 and the SEM images indicates that the SS and UVS processes can be separated into
8 three regimes in sequence: rubbing, plowing, and cutting. The material chips that were
9 generated in the cutting regime for SS and UVS were visible in enlarged SEM images
10 V and VII. For the SS process, materials were removed by rubbing, plowing, and
11 cutting when the scratch distance was 0–9 μm , 9–28 μm , and 28–70 μm , respectively.
12 However, for the UVS process, the scratch distance of the three regimes was 0–4 μm ,
13 4–15 μm , and 15–70 μm , respectively. Therefore, the UVS contributes to a shorter
14 scratch distance of the rubbing and plowing compared with the SS. Figure 4(a) and (b)
15 shows the AFM image and cross section that corresponds to the end of the machined
16 nanochannel (III) in Figure 3. The inserted SEM image in Figure 4(a) reveals the
17 nanochannel morphology that is marked in a dotted yellow rectangle. Figure 4(b) shows
18 that the machined depth at the end of the obtained nanochannel was ~ 60 nm. No cracks
19 and other brittle fracture were visible in Figure 4(a) [30], which means that the sample
20 materials were expelled in the ductile regime when the applied normal load ranged from
21 0 to 300 μN .

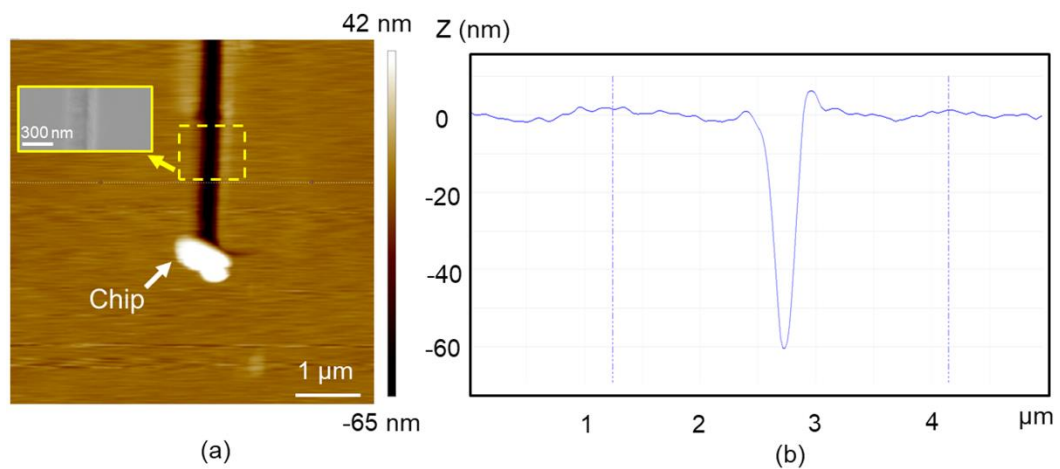


1

2 Figure 3. Nanoscratching tests with increasing normal load. (a,b) Horizontal force recorded during

3 SS and UVS, respectively. (c) Normal load along a scratching length of 70 μm . Inserts display

4 SEM images that correspond to the fabricated nanochannel.



5

6 Figure 4. (a) AFM image and (b) cross section of nanochannel end in Figure 3 (III).

7 3.2 Nanochannel morphology

1 The effect of scratching approaches, such as SS and UVS, on the machined
 2 nanochannel morphology was studied by SEM and AFM. Figure 5(a) and (b) provides
 3 an SEM image of the nanochannel that was fabricated by SS and UVS with normal load
 4 of 200 μN , respectively. The enlarged image in Figure 5(a) shows that a long curved
 5 segmental chip was generated at the end of the nanochannel. In contrast, the chip that
 6 formed at the end of the nanochannel that was fabricated by using UVS was a granular
 7 chip (Figure 5(b)). The inserted schematic diagrams in Figure 5(a) and (b) depict the
 8 material removal state that was fabricated by using the SS and UVS approaches,
 9 respectively. The observed SEM results show that the chip that was generated by using
 10 SS was longer than that formed by UVS. For the UVS process, a simplified elastic
 11 contact model was used to investigate the tip-sample interaction in the previous studies
 12 [25,31]. The relationship between the interaction force and tip-sample distance (d) can
 13 be calculated as follows:

$$14 \quad F(d) = \frac{E^* A^3}{R} - \left(\frac{3\pi}{2} \sigma E^* A^3 \right)^{1/2} - F_{\text{att}} \quad (2)$$

15 where R is the radius of the tip, and d is the distance between the tip and sample. σ is
 16 the adhesion energy defining as the work per unit area of contact required to separate
 17 two solid surfaces, which is assumed as 360 mJ/m^2 . The long-range attraction force
 18 (F_{att}) can be neglected in this study [32]. A is the radius of the tip-sample contact area
 19 and it can be estimated by $A^2 \approx Rd$. Thus, the Eq. (2) can be further expressed as follows:

$$20 \quad F(d) = E^* (Rd^3)^{1/2} - \left(\frac{3\pi}{2} \sigma E^* \right)^{1/2} (Rd)^{3/4} - F_{\text{att}} \quad (3)$$

21 The effective elasticity (E^*) can be expressed as follows:

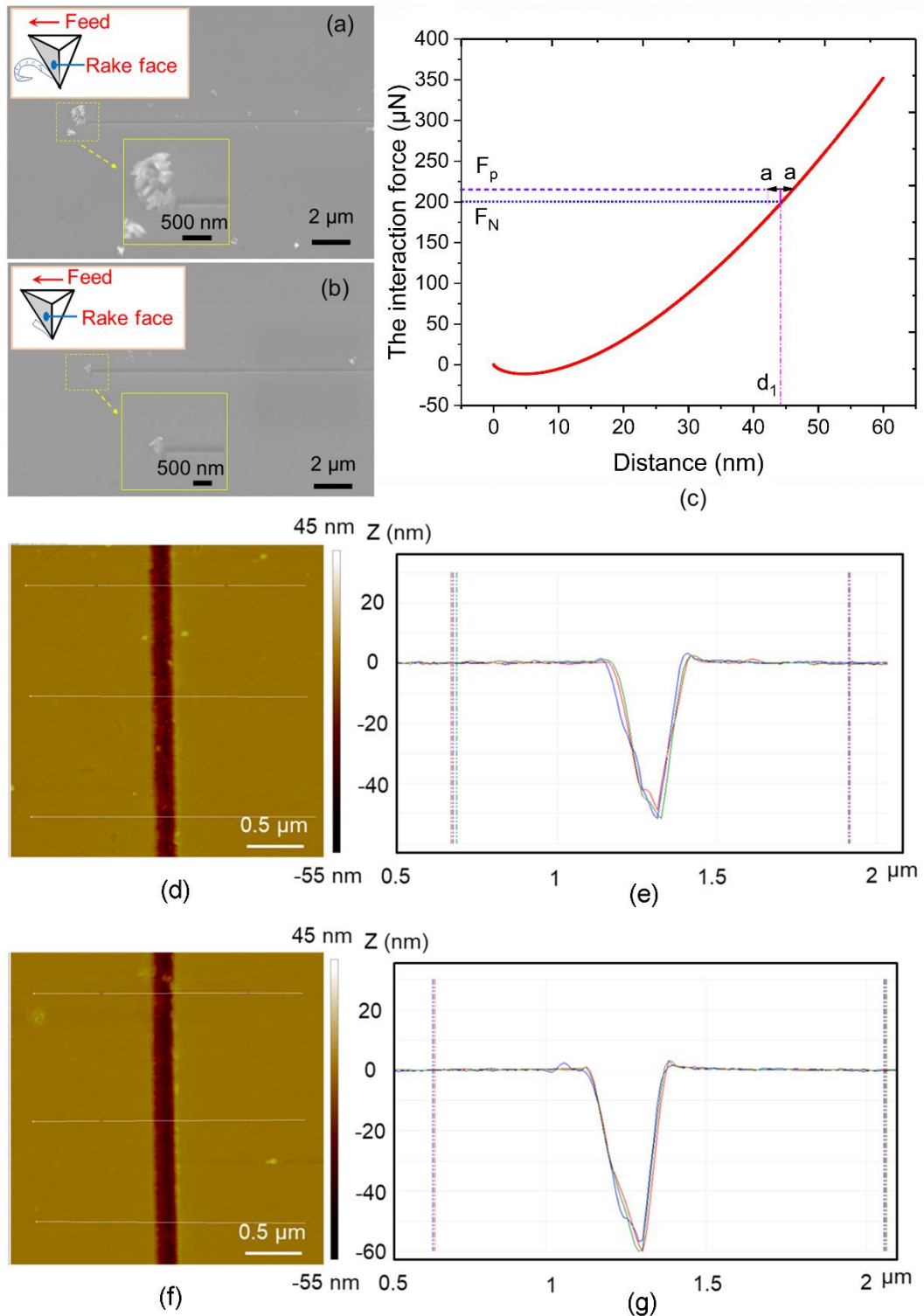
$$\frac{1}{E^*} = \frac{1-\nu_t^2}{E_t} + \frac{1-\nu_s^2}{E_s} \quad (4)$$

where E_t and ν_t , E_s and ν_s are Young's modulus and Poisson's ratio of the tip and sample, respectively, which is 1120 GPa, 0.12 [33], 127 GPa and 0.25 [34]. Applying Eqs (3) and (4), the force–distance relationship can be obtained as shown in Figure 5(c). F_N in Figure 5(c) is the setting normal load which is 200 μN in this study, the tip–sample distance (d_1) corresponding to the F_N is calculated to be 44.6 nm. The amplitude of the ultrasonic vibration (a) is 1.5 nm, as shown in Figure 5(c), which can introduce ± 1.5 nm change into tip–sample distance. Thus, the maximum tip–sample distance can be obtained by $d_2=d_1+1.5$, which is 46.1 nm. According to Eq. (3), the interaction force between tip and sample at the maximum tip–sample distance (F_p) is calculated to be 219 μN . The energy applied by the tip during nanoscratching can be obtained from the interaction force between the tip and sample multiplying the cutting depth, which can be estimated as follows [35]:

$$E = F_p \cdot D \quad (5)$$

where F_p and D is the interaction force and machined depth, respectively. In this study, the machined depth for SS and UVS is 50 nm and 60 nm respectively when the setting normal load is 200 μN . Applying Eqs (3)-(5), the calculated energy that applied by the tip for UVS (E_{UVS}) and SS (E_{SS}) is 1.314×10^{-8} mJ and 1×10^{-8} mJ, respectively. Thus, the energy applied by UVS (E_{UVS}) is approximately 1.3 times of that for SS (E_{SS}). The higher input energy that was caused by ultrasonic vibration in UVS may contribute to the fracturing of the formed chips compared with the SS process. The AFM images of the nanochannels that were fabricated by using SS and UVS with a normal load of 200

1 μN are shown in Figure 5(d) and (f). There was almost no pile-up for the obtained
2 nanochannels. Figure 5(e) and (g) shows the cross-sections that correspond to the
3 nanochannels as shown in Figure 5(d) and (f), respectively. The experimental results
4 show that the nanochannel depth that was obtained by using UVS was deeper compared
5 with that fabricated by the SS approach.



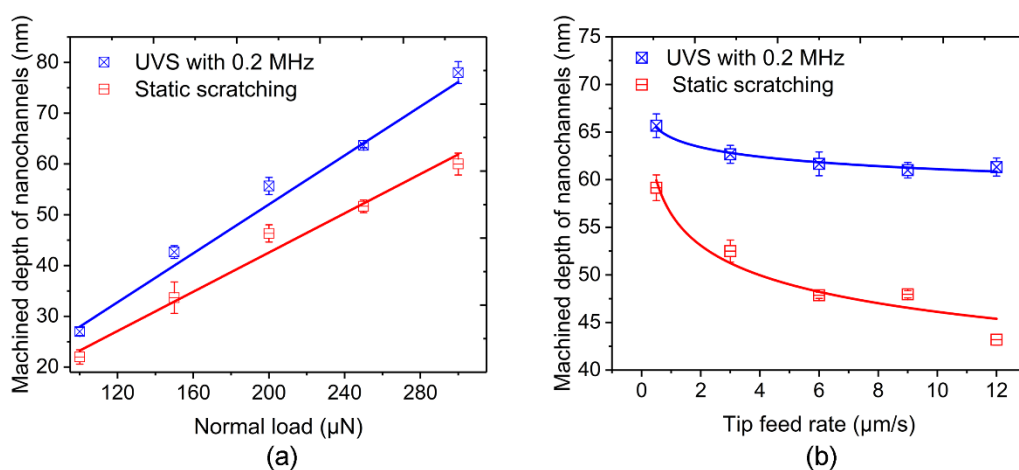
1

2 Figure 5. SEM images of nanochannels fabricated using (a) SS and (b) UVS at 0.2 MHz. (c) The
 3 interaction force between the tip and sample. AFM images and corresponding cross sections of
 4 nanochannels fabricated using (d,e) SS, (f,g) UVS of 0.2 MHz.

5

To understand the effect of the machining approaches on the nanochannel

1 dimensions, we conducted the SS and UVS processes with a normal load from 50 to
 2 300 μN and a spacing of 50 μN . Figure 6(a) shows that the machined depth increased
 3 with an increase in applied normal load for scratching by using SS and UVS. Figure
 4 6(a) shows that the machined depth of the UVS was deeper than that of the SS at the
 5 same applied normal load. The workpiece underwent an ultrasonic vibration with a
 6 given amplitude for UVS, which led to a relative motion between the tip and workpiece
 7 in the vertical direction during scratching. Thus, the machined depth was deeper in this
 8 scenario compared with scratching by SS. Similarly, the nanochannel depth that was
 9 scratched by using UVS was deeper than that when using SS when machining with the
 10 same tip feed rate (Figure 6(b)). Figure 6(b) shows that the machined depth decreased
 11 with an increase in feed rate for the SS and UVS approach. A higher feed rate resulted
 12 in a relatively large sample material strain rate during scratching, which increased the
 13 contact pressure between the tip and sample [36]. Thus, the machined depth was
 14 shallow at a larger feed rate to balance the constant normal load.



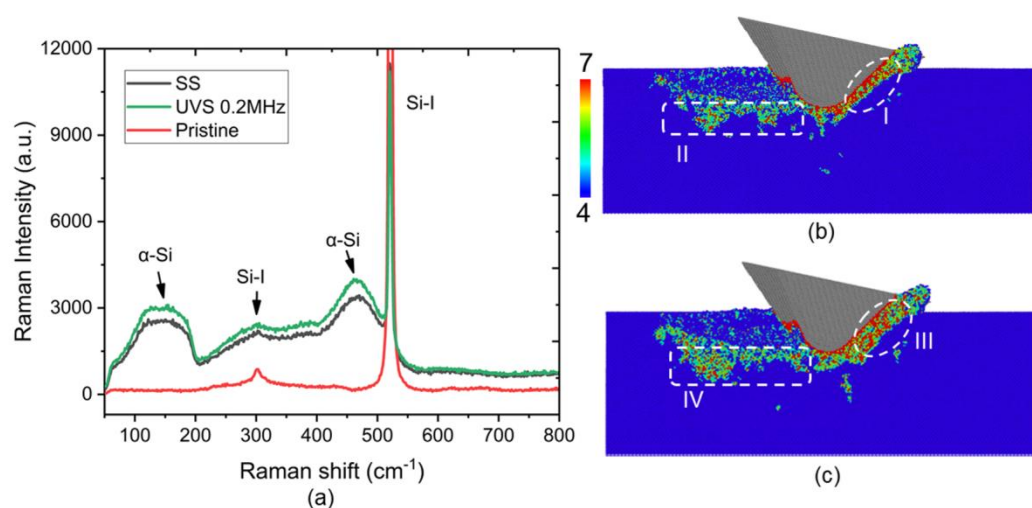
15
 16 Figure 6. Relationship between machined depth of nanochannels and (a) applied normal load, (b)
 17 tip feed rate when machining using SS and UVS approaches.

18 3.3 Nanochannel phase transformation

1 Figure 7(a) shows the Raman spectra of the nanostructures that were machined
2 by using SS and UVS. Pristine nanostructures were used compared with the machined
3 nanostructures. Three characteristic peaks in the SS and UVS spectrums were visible,
4 and included two broadband peaks at 150 cm^{-1} and 470 cm^{-1} and a strong and sharp
5 peak at 521 cm^{-1} . These characteristic peaks can be identified as the α -Si phase and Si-
6 I phase [37]. A series of phase transformations of single-crystal silicon occur during
7 machining [38]. The Si-I phase of the single-crystal silicon transforms into metallic Si-
8 II phase because of the high pressure. The metallic Si-II is unstable and will transform
9 into other phases. The transformation is determined by the rate of pressure release. The
10 Si-II phase will transform into Si-III and Si-XII phases at a relatively low rate of
11 pressure release, and into an α -Si phase when the release rate is high [39]. In this study,
12 the Raman spectra indicate that a layer of amorphous silicon was induced in the SS and
13 UVS process owing to the higher rate of pressure release.

14 Figure 7(a) shows that the Raman intensity of the UVS is stronger than that of
15 the SS. The Raman intensity is related to the amorphous layer thickness of single-
16 crystal silicon [37]. A stronger Raman intensity yields a thicker amorphous layer [40].
17 Thus, the Raman spectra reveal that the amorphous layer that is induced by UVS is
18 thicker than that by SS. To understand the phase transformation of SS and UVS, we
19 used an MD simulation approach to simulate the scratch process. An analysis of the
20 range of phase transformations was undertaken by the coordination number (n) in the
21 workpiece. Different phases of single-crystal silicon, including the diamond crystal
22 phase, bct-silicon, and β -silicon, were identified based on the coordination numbers.

1 Figure 7(b) and (c) shows the simulated phase transformation of SS and UVS,
 2 respectively. The contact area (I in Figure 7(b)) between the tip and sample was
 3 composed mainly of metastable atoms ($n = 7$) mixed with bct-silicon ($n = 5$) and β -
 4 silicon ($n = 6$), which was generated from the high pressure. The contact region for
 5 UVS (area III) was thicker than that for SS (area I). The bottom region of the
 6 nanochannel (II in Figure 7(b)) was composed of amorphous silicon atoms. The atoms
 7 were mainly bct-silicon ($n = 5$) and β -silicon ($n = 6$), which transformed from
 8 metastable atoms when the tip moved away and from the effect of unloading. A
 9 comparison of the bottom region of the nanochannel scratched by using SS (II in Figure
 10 7(b)) and UVS (IV in Figure 7(c)) showed that region IV was thicker. The MD
 11 simulations revealed that the amorphous layer that was induced by UVS was thicker,
 12 which agrees well with the Raman spectra.



13
 14 Figure 7. (a) Raman spectra of nanostructures machined using SS and UVS. Phase transformation
 15 of nanochannel simulated via MD: (b) SS and (c) UVS.

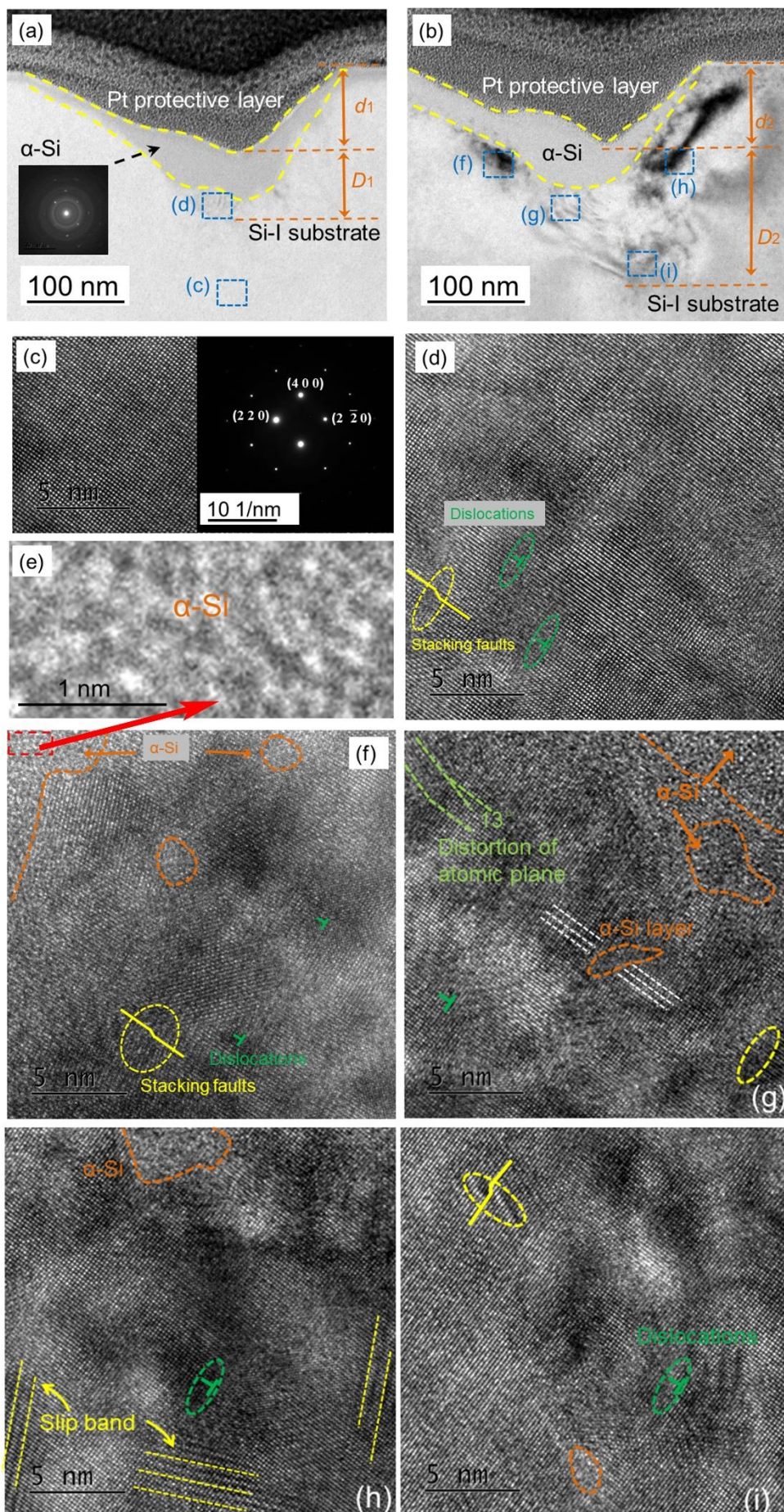
16 3.4 Subsurface damage of nanochannels

17 We used TEM to investigate the subsurface damage mechanism of single-crystal

1 silicon during ductile-machining using the SS and UVS approach. As shown in Figure
2 8(a) and (b), cross sections of the nanochannels that were scratched by SS and UVS,
3 which were termed channels I and II, respectively, were detected by TEM. A layer of
4 amorphous silicon was induced beneath the machined nanochannel, evidenced by the
5 diffraction pattern in Figure 8(a) [41,42]. Figure 8(a) and (b) shows that the amorphous
6 layer for channel II is thicker than that for channel I. The results indicate agreement
7 between the Raman spectra and TEM observations. The machined depths for channel I
8 (d_1 in Figure 8(a)) and II (d_2 in Figure 8(b)) are identical at ~ 80 nm. Furthermore, the
9 depths of subsurface damage for channel I (D_1) and II (D_2) are ~ 70 nm and 140 nm,
10 respectively. The TEM observation indicates that the UVS will induce a larger
11 subsurface damage compared with the SS approach.

12 To understand what happened in the subsurface, we performed high-resolution
13 TEM (HRTEM) in the regions beneath the induced amorphous layer, as pointed out in
14 Figure 8(a) and (b). The results that correspond to the selected areas in Figure 8(a) and
15 (b) are shown in Figure 8(c)–(i). We selected a region (c in Figure 8(a)) far from the
16 affected area as a reference to prove that subsurface damage was induced by the scratch.
17 As shown in Figure 8(c), no crystal defects existed in the pristine material. The
18 diffraction pattern that corresponds to the region, which is also provided in Figure 8(c),
19 illustrates strong lattice diffraction. The result indicates a single-crystal structure [21].
20 Hence, on the basis of the HRTEM and diffraction pattern of the pristine material, the
21 sample was single crystal without defects before machining, and any subsurface
22 damage after machining was caused by scratching.

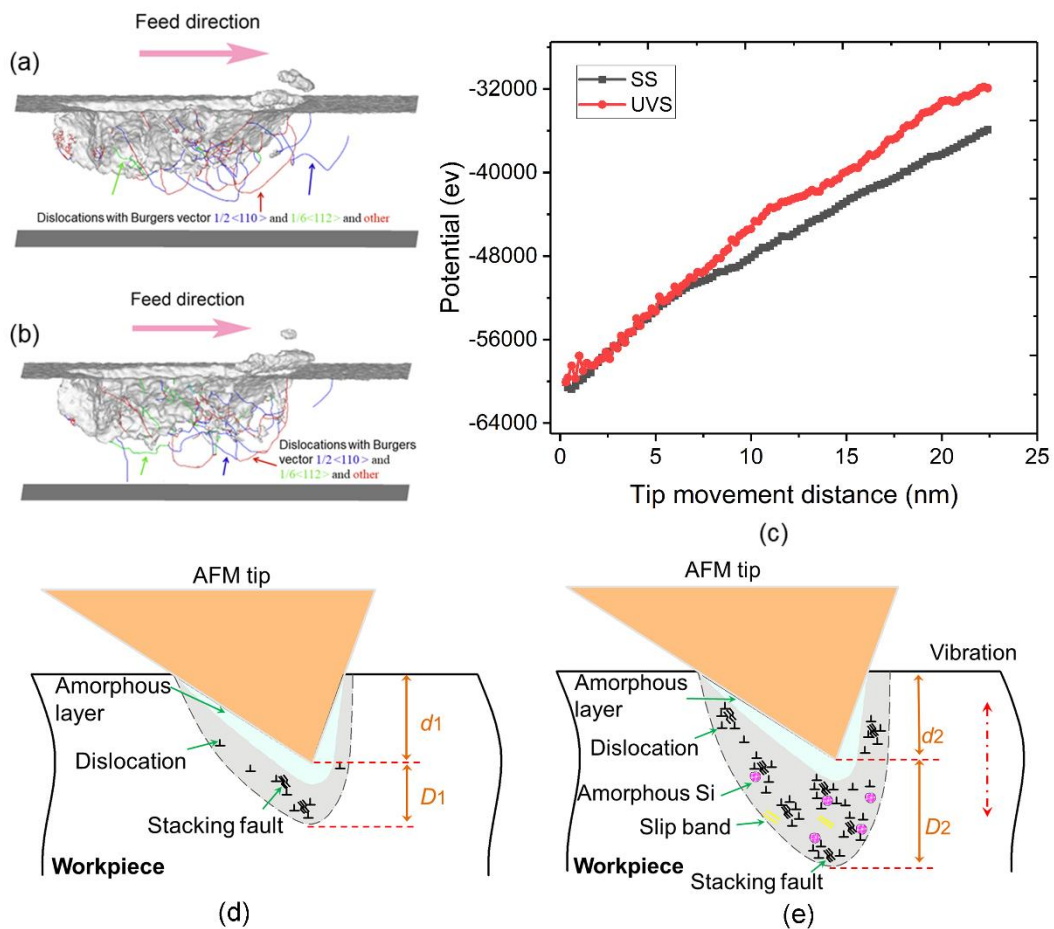
1 Figure 8(d) shows the HRTEM image of the area (*d* in Figure 8(a)). Dislocations
2 and stacking faults were induced for channel I during SS. The high pressure and shear
3 stress that were generated by SS contribute to these crystal defects [43]. Figure 8(f)–(i)
4 presents the HRTEM images that correspond to the marked areas in Figure 8(b).
5 Dislocations and stacking faults are also visible in Figure 8(f), furthermore, the enlarged
6 image (Figure 8(e)) of the area in Figure 8(f) is indicative of amorphous silicon [21].
7 The rapid release of pressure and an increase in defect concentration, such as
8 dislocations and stacking faults, facilitate amorphous phase formation [39, 44].
9 HRTEM images of the subsurface of channel II in Figure 8(g) and (h) reveal that in
10 addition to dislocations, stacking faults and amorphous silicon are induced, distortion
11 of atomic plane (Figure 8(g)) and slip band (Figure 8(h)) do exist in the plastic-
12 deformation zone [45,46]. Figure 8(i) shows atomic-scale defects, including
13 dislocations, stacking faults, and amorphous silicon. The HRTEM results demonstrate
14 that the plastic deformation mechanism under SS is different with UVS. For the SS
15 approach, only pressure-induced defects, such as dislocation and stacking faults were
16 observed. However, for UVS, in addition to these defects, a small amount of amorphous
17 phase, slip band, and distortion of atomic plane was identified in the damage area.
18 Furthermore, the depth of subsurface damage that was induced by UVS was deeper
19 than that for the SS.



1 constant at 293 K. Thus, we eliminated the effect of heat-generation energy in this study.
2 The separation energy for new surface generation can be calculated from $E = e\gamma\left(\frac{1}{h}\right)$,
3 where, e , γ , and h are the surface energy of the sample material, relief angle of the tip,
4 and the undeformed chip thickness, respectively [48]. The undeformed chip thickness
5 for SS was the same as that for UVS for an identical machined depth. Because the e , γ ,
6 and h , were the same, there was no difference in surface generation energy for SS and
7 UVS. Thus, more material disorder energy was exerted on the workpiece for UVS than
8 SS and resulted in a relatively large subsurface damage.

9 According to the TEM and MD simulation, we proposed schematic diagrams of
10 subsurface damage for nanochannels that were fabricated by using SS and UVS, as
11 shown in Figure 9(d) and (e). SS and UVS yielded a layer of amorphous silicon during
12 machining. Dislocation and stacking faults were present in the subsurface of the
13 channels that were machined by SS and UVS because of the high pressure and shear
14 stress. More atomic defects, such as atomic-plane distortion, local amorphization, and
15 slip bands were induced in the UVS (Figure 9(e)). Owing to a higher material disorder
16 energy, the subsurface damage that was caused by UVS (Figure 9(e)) was deeper than
17 SS (Figure 9(d)). The subsurface damage from UVS at the nanoscale was inconsistent
18 with that caused by the UVM at the macro- or microscale. UVM at the macro- and
19 microscale facilitated shallow subsurface damage compared with conventional static
20 machining [10-13]. The sample material during machining experiences plastic
21 deformation before it fractures. The plastic deformation is controlled by dislocation
22 motion. For macro- and microscale-UVM, the embrittlement of sample material that

1 was caused by dislocation immobilization and dislocation avalanche was regarded as
 2 the reason for a relatively shallow subsurface damage [14]. However, for nanoscale-
 3 UVS, the induced dislocations were less than those generated by microscale-UVM. The
 4 mobile dislocations extended inside the sample material more easily compared with the
 5 microscale-UVM, rather than being trapped and converted to immobile dislocations
 6 that distribute close to the machined surface. Thus, the material was more plastic during
 7 nanoscale-UVS compared with macroscale-UVM, which led to a relatively deep
 8 subsurface damage. Our experimental results indicate that the UVM was unsuitable for
 9 machining when the machined depth reached the nanoscale when aiming to suppress
 10 the subsurface damage.



11
 12

Figure 9. Distribution of dislocations obtained by MD simulation of single-crystal silicon

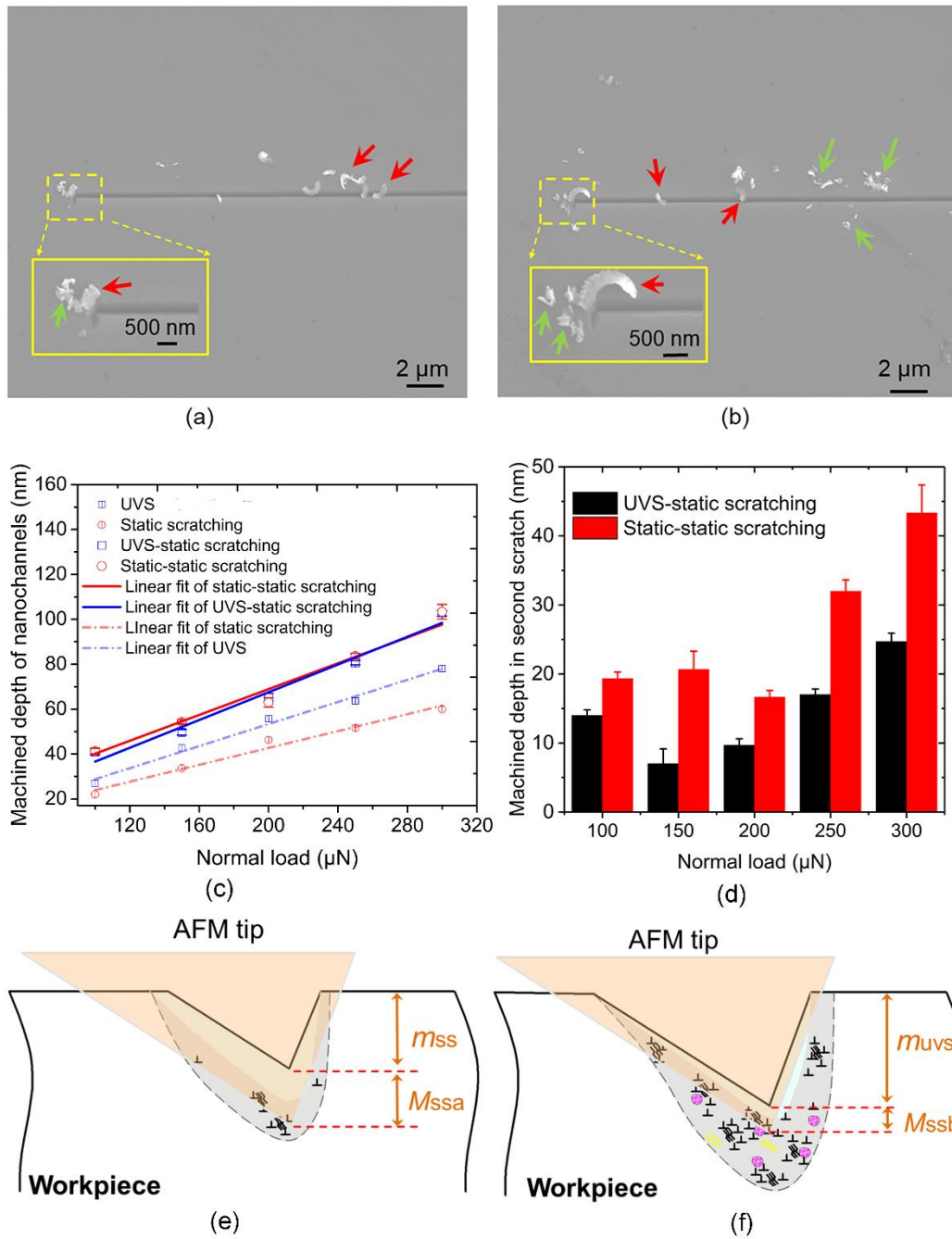
1 machining with (a) SS and (b) UVS. (c) Potential-energy evolution versus tip-movement distance
2 obtained by MD simulation. Schematic diagrams of subsurface damages for nanochannels
3 fabricated using (d) SS and (e) UVS, respectively.

4 **3.5 Effect of subsurface damage on machining mechanism**

5 To investigate the influence of subsurface damage on the machining mechanism,
6 we repeated the scratch process on the already machined nanochannels, which was
7 termed double-pass scratching in this study. The experimental details of the double-
8 pass scratching were introduced in Section 2.1. Two kinds of double-pass scratch
9 approaches were conducted: (i) the first and second scratches were both achieved by
10 static scratch and was defined static-static scratching (SS–SS) and (ii) the first and
11 second scratches were achieved by UVS and static scratching, respectively, and was
12 termed UVS-static scratching (UVS–SS). Figure 10(a) and (b) shows the SEM images
13 of the nanochannels that were machined by SS–SS and UVS–SS. Curved chips
14 (indicated by red arrows) formed during the second scratch process in Figure 10(a) and
15 (b). The long curved segmental chips (indicated by green arrows) in Figure 10(a) and
16 the granular chips in Figure 10(b) were generated during the first scratch, as discussed
17 in Section 3.2. A comparison of the curved chips with the chips that were generated in
18 the first scratch showed that the sample material plasticity improved after the first
19 scratch [49]. The expelled materials in the second scratch process were mainly
20 amorphous silicon and single-crystal silicon with many atomic defects. The amorphous
21 silicon and atomic defects, such as dislocation and stacking faults, facilitated material
22 removal in the plastic regime during the second scratch [50-52].

23 Figure 10(c) shows the relationship between the machined depth of the

1 nanochannel that was fabricated by using SS–SS and UVS–SS and the applied normal
2 load. Therefore, the machined depth increased linearly with an increase in applied
3 normal load. The machined depth of the SS–SS was almost identical to that of the UVS–
4 SS. We discussed the machined depth of the SS and UVS in Section 3.2 and reported
5 that the machined depth of the UVS was deeper than that of the SS. We calculated the
6 machined depth during the second scratch process, as shown in Figure 10(d). The
7 machined depth during the second scratch for SS–SS was larger than that for UVS–SS.
8 A previous study has shown that the sample material is significantly harder than the
9 pristine material after plastic deformation owing to the induced dislocations [48]. In the
10 first scratch process, the TEM results revealed that more atomic defects resulted from
11 UVS than SS, which led to a harder sample material for UVS–SS compared with SS–
12 SS in the second scratch. Therefore, the machined depth in the second scratch for SS–
13 SS was large compared with the UVS–SS. On the basis of the analysis, we provided
14 schematic diagrams of the double-pass scratching for SS–SS and UVS–SS in Figure
15 10(e) and (f), respectively. In the first scratch, the machined depth for the SS–SS (m_{ss}
16 in Figure 10(e)) was smaller than that for UVS–SS (m_{uvs} in Figure 10(f)). However, in
17 the second scratch, owing to the effect of subsurface damage that was induced by the
18 first scratch, the machined depth for the SS–SS (M_{ssa}) was larger compared with the
19 UVS–SS (M_{ssb}). The total machined depth of the nanochannel that was fabricated by
20 the two double-pass scratch approaches was approximately identical.



1

2 Figure 10. SEM images of nanochannels fabricated using double scratching approach: (a) SS-SS,

3 (b) UVS-SS. (c) Relationship between machined depth and normal load when machining using

4 double scratching. (d) Machined depth in second machining process for different normal loads.

5 Schematic diagrams of subsurface damage for (e) SS-SS and (f) UVS-SS, respectively.

6

7 4. Conclusions

8 We investigated the subsurface damage mechanism of hard-brittle material (i.e.,

1 single-crystal silicon) during ductile-machining using UVS. The investigation involved
2 a study of the material removal state, morphology, and dimensions of the machined
3 nanochannel, and the effect of subsurface damage on the scratch outcomes. Our major
4 findings were given as follows:

- 5 • Single-crystal silicon was removed by rubbing, plowing, and cutting in sequence
6 with an increase in normal load. Compared with conventional static nanoscratching,
7 the UVS led to a deeper machined depth and a shorter chip.
- 8 • The TEM, Raman spectroscopy, and MD simulation demonstrated that the
9 subsurface damage caused by UVS was deeper than that caused by static
10 nanoscratching owing to a larger material disorder energy. Compared with macro-
11 and microscale UVM, the material was more plastic during nanoscale-UVS, which
12 led to an opposite phenomenon of subsurface damage.
- 13 • The UVS resulted in more atomic defects, such as local amorphization, slip band,
14 and distortion of the atomic plane in addition to dislocation and stacking faults
15 compared with static nanoscratching.
- 16 • By using the double-pass scratch approach, we verified that the silicon was
17 significantly harder than the pristine material after plastic deformation. The
18 machined depth in the second scratch for SS–SS was relatively large compared with
19 the UVS–SS owing to fewer induced dislocations.

20 This work showed the subsurface damage mechanism of single-crystal silicon during
21 ductile-machining using UVS. Different from the microscale UVM, we found that the
22 nanoscale UVM induced deeper subsurface damage compared with conventional static
23 machining. Therefore, we believe this could provide an instruction that UVM may be
24 not a good choice to suppress subsurface damage of hard–brittle materials (such as

1 silicon) when the machined depth reaches to the nanoscale.

2

3 **Acknowledgements**

4 The authors gratefully acknowledge the financial supports of the National Natural
5 Science Foundation of China (51911530206, 52035004), Natural Science Foundation
6 of Heilongjiang Province of China (YQ2020E015), Self-Planned Task (NO.
7 SKLRS202001C) of State Key Laboratory of Robotics and System (HIT) and “Youth
8 Talent Support Project” of the Chinese Association for Science and Technology.

9

1 References

- 2 [1] J. Yin, W. Gao, Z. Zhang, Y. Mai, A. Luan, H. Jin, J. Jian. Q. Jin, Batch microfabrication of highly
3 integrated silicon-based electrochemical sensor and performance evaluation via nitrite water
4 contaminant determination, *Electrochimica Acta* 335 (2020) 135660.
- 5 [2] J. Li, D. Geng, D. Zhang, W. Qin, Y. Jiang, Ultrasonic vibration mill-grinding of single-crystal
6 silicon carbide for pressure sensor diaphragms, *Ceramic International* 44 (2018) 3107-3112.
- 7 [3] K. Samit, A. Katiyar, A. Raychaudhuri, One-dimensional Si/Ge nanowires and their
8 heterostructures for multifunctional applications-a review, *Nanotechnology* 28 (2017), 092001.
- 9 [4] S. Jenie, S. Plush, N. Voelcker, Recent advances on luminescent enhancement-based porous
10 silicon biosensors, *Pharmaceutical Research* 33 (2016) 2314-2336.
- 11 [5] Y. Geng, Y. Yan, J. Wang, Y. Zhuang, Fabrication of nanopatterns on silicon surface by combining
12 AFM-based scratching and RIE methods, *Nanomanufacturing and Metrology* 1 (2018) 225-235.
- 13 [6] A. Rosa, A. Leonhardt, L. Souza, L. Lima, M. Santos, L. Manera, J. Diniz, A novel self-aligned
14 double patterning integrated with Ga⁺ focused ion beam milling for silicon nanowire definition,
15 *Microelectronic Engineering* 237 (2021) 111493.
- 16 [7] E. Moataz, T. Mitarai, A. Tomohiro, M. Yasuyuki, N. Nobuhiko, Fabrication of Si photonic
17 waveguides by electron beam lithography using improved proximity effect correction, *Japanese*
18 *Journal of Applied Physics* 59 (2020) 126502.
- 19 [8] Z. Zhao, E. Jelenković, G. Xiao, Z. Zhuang, S. To, Hydrogen Ion Implantation Induced Cutting
20 Behavior Variation in Plunge Cutting of the Monocrystalline Silicon, *Nanomanufacturing and*
21 *Metrology* (2021) <https://doi.org/10.1007/s41871-020-00086-z>.
- 22 [9] Q. Fang, L. Zhang, Prediction of the threshold load of dislocation emission in silicon during
23 nanoscratching, *Acta Materialia* 61 (2013) 5469-5476.
- 24 [10] Z. Yang, L. Zhu, G. Zhang, C. Ni, B. Lin, Review of ultrasonic vibration-assisted machining in
25 advanced materials, *International Journal of Machine Tools & Manufacture* 156 (2020) 103594.
- 26 [11] Y. Ahmed, W. Cong, M.R. Stanco, Z. Xu, Z. Pei, C. Treadwell, Y. Zhu, Z. Li, Rotary ultrasonic
27 machining of alumina dental ceramics: a preliminary experimental study on surface and subsurface
28 damages, *Journal of Manufacturing Science and Engineering* 134 (2012) 064501.

- 1 [12] J. Wang, J. Zhang, P. Feng, P. Guo, Damage formation and suppression in rotary ultrasonic
2 machining of hard and brittle materials: a critical review, *Ceramics International* 44 (2018) 1227-
3 1239.
- 4 [13] F. Lakhdari, D. Bouzid, N. Belkhir, V. Herold, Surface and subsurface damage in Zerodur® glass
5 ceramic during ultrasonic assisted grinding, *International Journal of Advanced Manufacturing*
6 *Technology* 90 (2017) 1993-2000.
- 7 [14] B. Zhang, J. Yin, The ‘skin effect’ of subsurface damage distribution in materials subjected to
8 high-speed machining, *International Journal of Extreme Manufacturing* 1 (2019) 012007.
- 9 [15] C. Zhang, P. Feng, J. Zhang, Ultrasonic vibration-assisted scratch-induced characteristics of C-
10 plane sapphire with a spherical indenter, *International Journal of Machine Tools & Manufacture* 64
11 (2013) 38-48.
- 12 [16] Z. Liang, X. Wang, Y. Wu, L. Xie, L. Jiao, W. Zhao, Experimental study on brittle-ductile
13 transition in elliptical ultrasonic assisted grinding (EUAG) of monocrystal sapphire using single
14 diamond abrasive grain, *International Journal of Machine Tools & Manufacture* 71 (2013) 41-51.
- 15 [17] Y. Yan, Y. Geng, Z. Hu, Recent advances in AFM tip-based nanomechanical machining,
16 *International Journal of Machine Tools & Manufacture* 99 (2015) 1-18.
- 17 [18] H. Liu, Y. Guo, D. Li, P. Zhao, J. Wang, Material Removal Mechanism of FCC Single-crystalline
18 Materials at nano-scales: Chip Removal and Ploughing, *Journal of Materials Processing Technology*
19 (2021) doi: <https://doi.org/10.1016/j.jmatprotec.2021.117106>.
- 20 [19] S. Lee, Analysis of ductile mode and brittle transition of AFM nanomachining of silicon,
21 *International Journal of Machine Tools & Manufacture* 61 (2012) 71-79.
- 22 [20] J. Guo, C. Xiao, B. Peng, L. Qian, Tribochemistry-induced direct fabrication of nondestructive
23 nanochannels on silicon surface, *RSC Advances* 5 (2015) 100769.
- 24 [21] J. Wang, Y. Yan, Z. Li, Y. Geng, Towards understanding the machining mechanism of the atomic
25 force microscopy tip-based nanomilling process, *International Journal of Machine Tools and*
26 *Manufacture* 162 (2021) 103701.
- 27 [22] S. Park, M. Mostofa, C. Park, M. Mehrpouya, S. Kim, Vibration assisted nano mechanical
28 machining using AFM probe, *CIRP Annals – Manufacturing Technology* 63 (2014) 537-540.
- 29 [23] J. Deng, L. Zhang, J. Dong, P. Cohen, AFM-based 3D nanofabrication using ultrasonic vibration

- 1 assisted nanomachining, *Journal of Manufacturing Processes* 24 (2016) 195-202.
- 2 [24] J. Deng, J. Dong, P. Cohen, Development and characterization of ultrasonic vibration assisted
3 nanomachining process for three-dimensional nanofabrication, *IEEE Transactions on*
4 *Nanotechnology*, 17 (2018) 559-566.
- 5 [25] Y. Geng, Y. Yan, Y. Zhuang, Z. Hu, Effects of AFM tip-based direct and vibration assisted
6 scratching methods on nanogrooves fabrication on a polymer resist, *Applied Surface Science* 356
7 (2015) 348-354.
- 8 [26] F. Stillinger, T. Weber. Computer simulation of local order in condensed phases of silicon.
9 *Physical Review B* 31 (1985) 5262-5271.
- 10 [27] Q. Tang, MD simulation of dislocation mobility during cutting with diamond tip on silicon,
11 *Materials Science in Semiconductor Processing* 10 (2007) 270-275.
- 12 [28] S. Plimpton, Fast parallel algorithms for short-range molecular dynamic, *Journal of*
13 *Computational Physics*, 117 (1995) 1-19.
- 14 [29] A. Stukowski, Visualization and analysis of atomistic simulation data with OVITO-the Open
15 Visualization Tool, *Modeling and Simulation in Materials Science and Engineering* 18 (2010)
16 015012.
- 17 [30] C. Li, Y. Zhang, G. Zhou, Z. Wei, L. Zhang, Theoretical modeling of brittle-to-ductile transition
18 load of KDP crystal on (001) plane during nanoindentation and nanoscratch tests, *Journal of*
19 *Materials Research and Technology* 9 (2020) 14142-14157.
- 20 [31] N.A. Burnham, R.J. Colton, H.M. Pollock, Interpretation of force curves in force microscopy,
21 *Nanotechnology* 4 (1993) 64-80.
- 22 [32] L. Zhang, J. Dong, P. Cohen, Material-insensitive feature depth control and machining force
23 reduction by ultrasonic vibration in AFM-based nanomachining, *IEEE Transactions*
24 *Nanotechnology* 12 (2013) 743-750.
- 25 [33] J. Philip, P. Hess, T. Feygelson, J. E. Butler, S. Chattopadhyay, K. H. Chen, L. C. Chen, Elastic,
26 mechanical, and thermal properties of nanocrystalline diamond films, *Journal of Applied Physics* 93
27 (2003) 2164-2171.
- 28 [34] X. Li, Y. Gao, P. Ge, L. Zhang, W. Bi, J. Meng, Nucleation location and propagation direction of
29 radial and median cracks for brittle material in scratching, *Ceramics International* 45 (2019) 7524-

- 1 7536.
- 2 [35] Z. Lin, Y. Hsu, A calculating method for the fewest cutting passes on sapphire substrate at a
3 certain depth using specific down force energy with an AFM probe, *Journal of Materials Processing*
4 *Technology* 212 (2012) 2321-2331.
- 5 [36] C. Li, F. Zhang, Y. Wu, X. Zhang, Influence of strain rate effect on material removal and
6 deformation mechanism based on ductile nanoscratch tests of Lu₂O₃ single crystal, *Ceramics*
7 *International* 44 (2020) 21486-21498.
- 8 [37] J. Yan, T. Asami, H. Harada, T. Kuriyagawa, Fundamental investigation of subsurface damage in
9 single crystalline silicon caused by diamond machining, *Precision Engineering* 33 (2009) 378-386.
- 10 [38] Y. Wu, H. Huang, J. Zou, L. Zhang, J. Delld, Nanoscratch-induced phase transformation of
11 monocrystalline Si, *Scripta Materialia* 63 (2010) 847-850.
- 12 [39] G. Gassilloud, C. Ballif, P. Gasser, G. Buerki, J. Michler, Deformation mechanisms of silicon
13 during nanoscratching, *Physica Status Solidi A-Applications and Materials Science* 202 (2005)
14 2858-2869.
- 15 [40] J. Yan, T. Asami, T. Kuriyagawa, Nondestructive measurement of machining-induced amorphous
16 layers in single-crystal silicon by laser micro-Raman spectroscopy, *Precision Engineering* 32 (2008)
17 186-195.
- 18 [41] T. Sumitomo, H. Huang, L. Zhou, J. Shimizu, Nanogrinding of multi-layered thin film
19 amorphous Si solar panels, *International Journal of Machine Tools & Manufacture* 51 (2011) 797-
20 805.
- 21 [42] X. Rao, F. Zhang, Y. Lu, X. Luo, F. Chen, Surface and subsurface damage of reaction-bonded
22 silicon carbide induced by electrical discharge diamond grinding, *International Journal of Machine*
23 *Tools & Manufacture* 154 (2020) 103564.
- 24 [43] A. Minor, E. Lilleodden, M. Jin, E. Stach, D. Chrzan, J. Morris, Room temperature dislocation
25 plasticity in silicon, *Philosophical Magazine* 85 (2005) 323-330.
- 26 [44] Z. Shi, J. Zhang, Q. Zhao, B. Guo, H. Wang, Transmission electron microscopy (TEM) study of
27 anisotropic surface damages in micro-cutting polycrystalline aluminate magnesium spinel (PAMS)
28 crystals, *Ceramics International* 46 (2020) 20570-20575.
- 29 [45] C. Li, X. Li, Y. Wu, F. Zhang, H. Huang, Deformation mechanism and force modelling of the

- 1 grinding of YAG single crystals, *International Journal of Machine Tools & Manufacture* 143 (2019)
2 23-37.
- 3 [46] R. Liu, M. Wang, Z. Li, P. Cao, T. Yuan, H. Zhu, Developing a high-strength Al-Mg-Si-Sc-Zr
4 alloy for selective laser melting: Crack-inhibiting and multiple strengthening mechanisms, *Acta*
5 *Materialia* 193 (2020) 83-98.
- 6 [47] J. Li, Q. Fang, L. Zhang, Y. Liu, Subsurface damage mechanism of high speed grinding process
7 in single crystal silicon revealed by atomistic simulations, *Applied Surface Science* 324 (2015) 464-
8 474.
- 9 [48] F. Fang, F. Xu, M. Lai, Size effect in material removal by cutting at nano scale, *International*
10 *Journal of Advanced Manufacturing Technology* 80 (2015) 591-598.
- 11 [49] C. Li, F. Zhang, Y. Piao, Strain-rate dependence of surface/subsurface deformation mechanisms
12 during nanoscratching tests of GGG single crystal, *Ceramics International* 45 (2019) 15015-15024.
- 13 [50] S. Goel, A. Kovalchenko, A. Stukowski, G. Cross, Influence of microstructure on the cutting
14 behaviour of silicon, *Acta Materialia* 105 (2016) 464-478.
- 15 [51] S. Chavoshi, S. Xu, X. Luo, Dislocation-mediated plasticity in silicon during nanometric cutting:
16 A molecular dynamics simulation study, *Materials Science in Semiconductor Processing* 51(2016)
17 60-70.
- 18 [52] S. Goel, X. Luo, A. Agrawal, R. Reuben, Diamond machining of silicon: A review of advances
19 in molecular dynamics simulation, *International Journal of Machine Tools & Manufacture* 88 (2015)
20 131-164.